Effects of Changes in Chemistry on Flex Bending Fatigue Behavior of Al-Based Amorphous Alloy Ribbons

CHUN-KUO HUANG and JOHN J. LEWANDOWSKI

The effects of changes in composition on the flow behavior and flex bending fatigue behavior of a series of Al-Gd-Ni-X (X = Fe or Co) amorphous alloy ribbons have been determined at 1 Hz at room temperature. It has been shown that the addition of Fe, Co, and Fe/Co combination into these materials increases the strength, T_g, and T_{x1} in addition to the activation energy for crystallization. The lowest strength (*i.e.,* 880 MPa) base alloy $Al_{87}Gd_6Ni_7$ exhibited the best low-cycle fatigue (LCF) and worst high-cycle fatigue (HCF) behavior, whereas the higher strength alloys (~1100 MPa) $Al_{85}Gd_6Ni_7Fe_2$ and $Al_{85}Gd_6Ni_7Fe_1Co_1$ exhibited worse LCF and better HCF behavior. The ratio of the stress amplitude at the fatigue limit at 1×10^6 cycles to uniaxial failure strength ranged from 0.25 to 0.37 (240 to 397 MPa), much higher than conventional aluminum alloys. These results are also compared with those obtained on other amorphous alloy ribbons.

DOI: 10.1007/s11661-011-0853-2

I. INTRODUCTION

A combination of good strength and low density (*i.e.*, specific strength) is a necessary requirement for structural materials, whereas damage tolerance and fatigue resistance are also critical. Amorphous and nanocrystalline aluminum alloys have attracted significant interest in recent years because of their high strength and low density.[1] Among the most studied Al-based amorphous alloys are the aluminum-rare earth-transition (Al-RE-TM) metal systems because of their good glass-forming ability and mechanical properties.[2–4] These alloys have been shown to exhibit strengths nearly twice that of conventional Al alloys (7075-T6:$\sigma_y \approx$ 500 MPa) with similar densities.[1] Recent work showed positive effects of Fe, Co, and Fe/Co additions to T_g, T_x, strength at different temperatures, and activation energy for crystallization for Al-Gd-Ni-X amorphous alloy ribbons.[5] However, essentially no fatigue data exist for these amorphous materials, although both high cycle fatigue (HCF) and fracture toughness data exist for nanocrystalline composites produced via devitrification.[6]

The mechanical properties of amorphous alloys have continued to receive great attention, with significant opportunities to improve fatigue performance. Some reports show that the fatigue limit of Zr-based metallic glasses is less than 10 pct of their ultimate tensile strength.[7,8] On the other hand, several studies including a recent review reveal that the fatigue limits of Pd-based and Zr-based metallic glasses are as high as crystalline metallic materials, 30 to 50 pct of their ultimate tensile strength (UTS).[9–14] Such differences in the fatigue limits of amorphous alloys have been proposed as a result of different loading conditions,[14] as well as because of the presence/absence of defects (*e.g.,* inclusions, crystalline regions, pores, *etc*).[11] Although the high elastic limit/strength of such systems might imply good fatigue resistance in the HCF regime, mixed results have been obtained.[7–15] Early work on amorphous wire ribbons revealed generally good HCF behavior,[16] whereas the behavior of bulk metallic glasses has been much more variable.[7–15]

In this article, fatigue tests on a series of Al-RE-TM amorphous alloy ribbons were performed under fully reversed flex bending fatigue conditions via cyclic bending over mandrels of different diameter. The wide range of mandrel sizes enables examination in both the low cycle fatigue and high cycle fatigue regimes. The fatigue performance is presented by cyclic stress/strain *vs* fatigue life curves (S-N curves) to examine the effects of systematic changes in chemical composition on fatigue performance.

II. EXPERIMENTAL PROCEDURES

The Al-based amorphous alloy ribbons with a thickness of 50 to 55 μm and a width of 1.7 to 1.9 mm were prepared by the Ames laboratory via melt spinning with a rotating chilled copper wheel at a tangential speed of 16 m/s. To investigate the effects of chemistry changes on fatigue properties, $Al_{86}Gd_6Ni_7Fe_1$, $Al_{86}Gd_6Ni_7Co_1$, $Al_{85}Gd_6Ni_7Fe_2$, and $Al_{85}Gd_6Ni_7Fe_1Co_1$ ribbons were produced by the addition of Fe/Co into the base alloy ($Al_{87}Gd_6Ni_7$). All the as-spun ribbons were confirmed fully amorphous by X-ray diffraction (XRD; X1; Scintag, Cupertino, CA) and by transmission electron spectroscopy (TEM; Tecnai F30; FEI, Hillsboro, OR). Basic mechanical properties of these ribbons tested at

CHUN-KUO HUANG, Graduate Student, and JOHN J. LEWANDOWSKI, Professor, are with the Department of Materials Science and Engineering, Case Western Reserve University, Cleveland, OH 44106-7204. Contact e-mail: jjl3@case.edu
Manuscript submitted February 24, 2011.
Article published online August 30, 2011

room temperature are provided in Table I.[5] The thermal stabilities and tensile properties of these alloys have been summarized elsewhere.[5]

Fatigue tests were performed in laboratory air at room temperature on the amorphous ribbon samples using a modified GE Fatigue Ductility Flex Tester according to ASTM Standard E 796-94.[17] This procedure has been used successfully on both thin sheet/foil specimens as well as small diameter wires/cables.[18–22] The ribbon fatigue specimens were subjected to a fixed cyclic strain amplitude via fully reversed bending (*i.e.,* $R = -1$) over a pair of steel mandrels. To minimize any heating that may arise because of high cyclic frequencies, a low loading frequency of 1 Hz was used.

Sample preparation for the fatigue experiments was as follows. Visual and optical microscope inspections were performed first to ensure uniformity of ribbon surfaces and edges. Laser confocal microscopy revealed surface roughness of 40 nm and 150 nm for the air and wheel side, respectively. Fatigue specimens approximately 30 mm long were selected from melt-spun ribbons exhibiting such uniformity. Each specimen was then attached to a small dead load (*e.g.,* <50 g) at both ends to provide stability from slipping out of the mandrels. Given the sample dimensions (*i.e.,* width: 1.7 mm, thickness: 55 μm), a minimal stress is produced (*e.g.,* 5.2 MPa) on the sample. Mandrel diameters used presently were 3.95 mm, 6.03 mm, 8.03 mm, 9.88 mm, 11.40 mm, 12.80 mm, and 19.0 mm. The ribbon/mandrel pair was cycled at 1 Hz to minimize any sample heating and cycled until failure was detected by a current/voltage break detector that provided a small direct current through the specimen. The fracture surfaces of the fatigue specimens were examined by scanning electron microscopy (SEM) (FEI Quanta 200) operated at 10 KV.

III. RESULTS

Ribbon samples from each composition were tested first by bending over a single mandrel to investigate their bend ductility at different mandrel sizes. The $Al_{87}Gd_6Ni_7$, $Al_{86}Gd_6Ni_7Fe_1$, and $Al_{86}Gd_6Ni_7Co_1$ ribbons exhibited no permanent deformation and no shear bands on the ribbon surfaces after bending over a mandrel of 3.95 mm in diameter, whereas the $Al_{85}Gd_6Ni_7Fe_2$ and $Al_{85}Gd_6Ni_7Fe_1Co_1$ ribbons revealed shear bands during SEM examination. All the ribbons showed shear bands on their surfaces after bending over a 1.95-mm diameter mandrel, but none of them failed. This finding indicates that these alloy chemistries may be able to tolerate high bending strains without failure. The bend test results are summarized in Table II, where the applied strain is calculated as $\frac{t}{D}$ where t is the thickness of the ribbon and D is the diameter of the mandrel.[20]

Also included in Table II are calculations for the applied stress. In the elastic regime, the applied stress can be calculated from $\sigma = E \times \varepsilon$ if the Young's modulus E is known. E was obtained from instrumented nanoindentation, which is also provided in Table I.

Figure 1 and Table III show the effects of changes in mandrel diameter on the number of cycles to failure of the various alloy ribbons.

The fatigue life increases with an increase in the mandrel diameter for each system because bending over a larger mandrel produces a smaller cyclic strain on the ribbons, as calculated in the discussion. The ribbons that did not fail after 1,000,000 cycles were removed from the flex fatigue machine and were examined in the SEM for any evidence of shear bending and/or damage.

An examination of the ribbon samples that failed in fatigue revealed similar features. Figures 2(a) and (b) show low-magnification SEM views of the fracture

Table I. Mechanical Properties of ~$Al_{87}Gd_6Ni_7$, $Al_{86}Gd_6Ni_7Fe_1$, $Al_{86}Gd_6Ni_7Co_1$, $Al_{85}Gd_6Ni_7Fe_2$, and $Al_{85}Gd_6Ni_7Fe_1Co_1$ Ribbons at Room Temperature

Alloy (at pct)	σ_f (MPa)	$\varepsilon_{c,f}$ (pct)	E (GPa)	E_c (GPa)	Hv (kg/mm^2)	$\sigma_{c,y}$ (MPa)	T_g [K (°C)]	T_{x1} [K (°C)]
$Al_{86}Gd_6Ni_7Fe_1$	1055	1.3	82.2	70.3 to 75.2	320	1050	471 (198)	497 (224)
$Al_{86}Gd_6Ni_7Co_1$	1075	1.3	82.4	70.2 to 75.0	325	1065	477 (204)	501 (228)
$Al_{85}Gd_6Ni_7Fe_2$	850	1.0	84.7	70.5 to 76.3	355	1160	523 (250)	539 (266)
$Al_{85}Gd_6Ni_7Fe_1Co_1$	950	1.1	84.5	70.7 to 76.0	330	1075	522 (249)	539 (266)
$Al_{87}Gd_6Ni_7$	880	1.1	81.6	70.0 to 74.2	300	970	441 (168)	462 (189)

σ_f: tensile fracture strength; E: Young's modulus measured via instrumented indentation; $\varepsilon_{c,f}$: calculated fracture strain; E_c: calculated Young's modulus; Hv: Vickers hardness number; $\sigma_{c,y}$: calculated compressive yield strength; T_g: glass transition temperature; T_{x1}: first crystallization temperature.

Table II. Summary of Bend Test Results on $Al_{86}Gd_6Ni_7Fe_1$, $Al_{86}Gd_6Ni_7Co_1$, $Al_{85}Gd_6Ni_7Fe_2$, and $Al_{85}Gd_6Ni_7Fe_1Co_1$ Ribbons at Room Temperature

Alloy (at pct)	D = 1.95 mm	ε_{max} (pct)	σ_{max} (MPa)	D = 3.95 mm	ε_{max} (pct)	σ_{max} (MPa)
$Al_{86}Gd_6Ni_7Fe_1$	shear bands	2.82	2318	no shear band	1.42	1167
$Al_{86}Gd_6Ni_7Co_1$	shear bands	2.87	2365	no shear band	1.39	1145
$Al_{85}Gd_6Ni_7Fe_2$	shear bands	2.87	2431	shear bands	1.40	1186
$Al_{85}Gd_6Ni_7Fe_1Co_1$	shear bands	2.82	2383	shear bands	1.39	1175
$Al_{87}Gd_6Ni_7$	shear bands	2.90	2366	no shear band	1.42	1159

surface of an $Al_{86}Gd_6Ni_7Co_1$ specimen tested to failure at 25,530 cycles with a mandrel diameter of 9.88 mm. The fatigue region shown in Figure 2(a) exhibits typical fatigue striations as shown in higher magnification in Figure 2(c). Such fatigue features are presented on both sides of the ribbons surface and suggest that fatigue cracks initiated from both the air and wheel side surfaces of the ribbon, with subsequent fatigue crack growth toward the center of the ribbon, followed by catastrophic failure. Overload regions exhibited a different appearance as shown in Figure 2(b). Higher magnification views of the overload region (Figure 2(d)) revealed major vein-like regions that propagated from the fatigue regions.

IV. DISCUSSION

The mechanical properties listed in Table I are generally consistent with previous work on amorphous aluminum alloys.[5] Although the alloying additions and chemistry changes shown seem to produce inconsistent results when the samples are tested in tension, the compressive yield strength estimated from the hardness reveals that the base $Al_{87}Gd_6Ni_7$ alloy possessed the lowest strength and additions of Fe and Co increased the compressive strength. This discrepancy likely relates to small defects that are sampled in the relatively large gage section of the tension samples (*i.e.,* 10 mm × 1 mm × 0.055 mm), as others have noted. Although scanning laser confocal microscopy revealed surface roughness of only 40 nm and 150 nm on the air and wheel side surfaces, respectively, other isolated individual defects (*e.g.,* pores, *etc.*) may not have been detected by this technique. In addition, it is clear that such alloying additions affect the magnitude of the Young's modulus *E*. Simple estimates of the upper bound and lower bound of Young's modulus via a weighted average of the constituents, as proposed by Zhang and Greer[23] and Wang *et al.*,[24] produce the values shown in Table I. Thus, in these systems, as in some others, the relative effects of alloying additions on some of the elastic constants can be estimated readily.

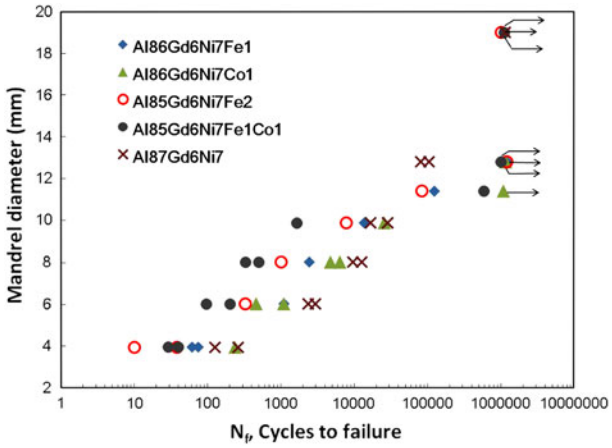

Fig. 1—Effect of mandrel diameter on the cycles to failure for Al-Gd-Ni-*X* (*X* = Fe or Co) amorphous alloy ribbons. The arrows indicate the sample did not fail.

The quasi-static bend over mandrel tests on the ribbons summarized in Table II reveal that bending over a small enough diameter mandrel will produce detectable yielding (*i.e.,* presence of shear bands) but not fracture on the surface of the ribbon. Although the data in Table II do not permit the calculation of the exact strain/stress required for initiation of shear bands in each of the alloy ribbons, the magnitude of stress is in the range of that obtained from the hardness tests. The magnitude of the strain for shear band observation is also similar to those shown elsewhere.[25,26] None of the ribbon samples failed after bending over either a 3.95-mm diameter mandrel or the 1.95-mm diameter mandrel, although the extent of shear banding was greater in the latter. This finding is consistent with much previous work[26] and is consistent with the general malleability of amorphous metals.

These observations of the strain/stress required for activation of shear bands can also be used to rationalize partially the fatigue behavior under the flex bending conditions conducted currently because the flex fatigue tests simply subject the ribbons to cyclic bend over

Table III. Effect of Mandrel Diameter on Cycles to Failure

Mandrel Diameter (mm)	$Al_{86}Gd_6Ni_7Fe_1$	$Al_{86}Gd_6Ni_7Co_1$	$Al_{85}Gd_6Ni_7Fe_2$	$Al_{85}Gd_6Ni_7Fe_1Co_1$	$Al_{87}Gd_6Ni_7$
3.95	61	234	10	29	125
3.95	74	—	38	40	260
6.03	1095	455	326	96	2361
6.03	—	1083	—	204	2961
8.03	2420	4703	1003	329	9607
8.03	—	6317	—	497	12709
9.88	13580	25530	7828	1653	16560
9.88	—	—	—	—	28783
11.4	123057	1178990 (DNF)	83356	586254	—
12.8	1209234 (DNF)	1158465 (DNF)	1209874 (DNF)	1013455 (DNF)	81808
12.8	—	—	—	—	104935
19.0	—	—	1012574 (DNF)	1114160 (DNF)	1150926 (DNF)

DNF denotes sample did not fail after number of cycles listed.

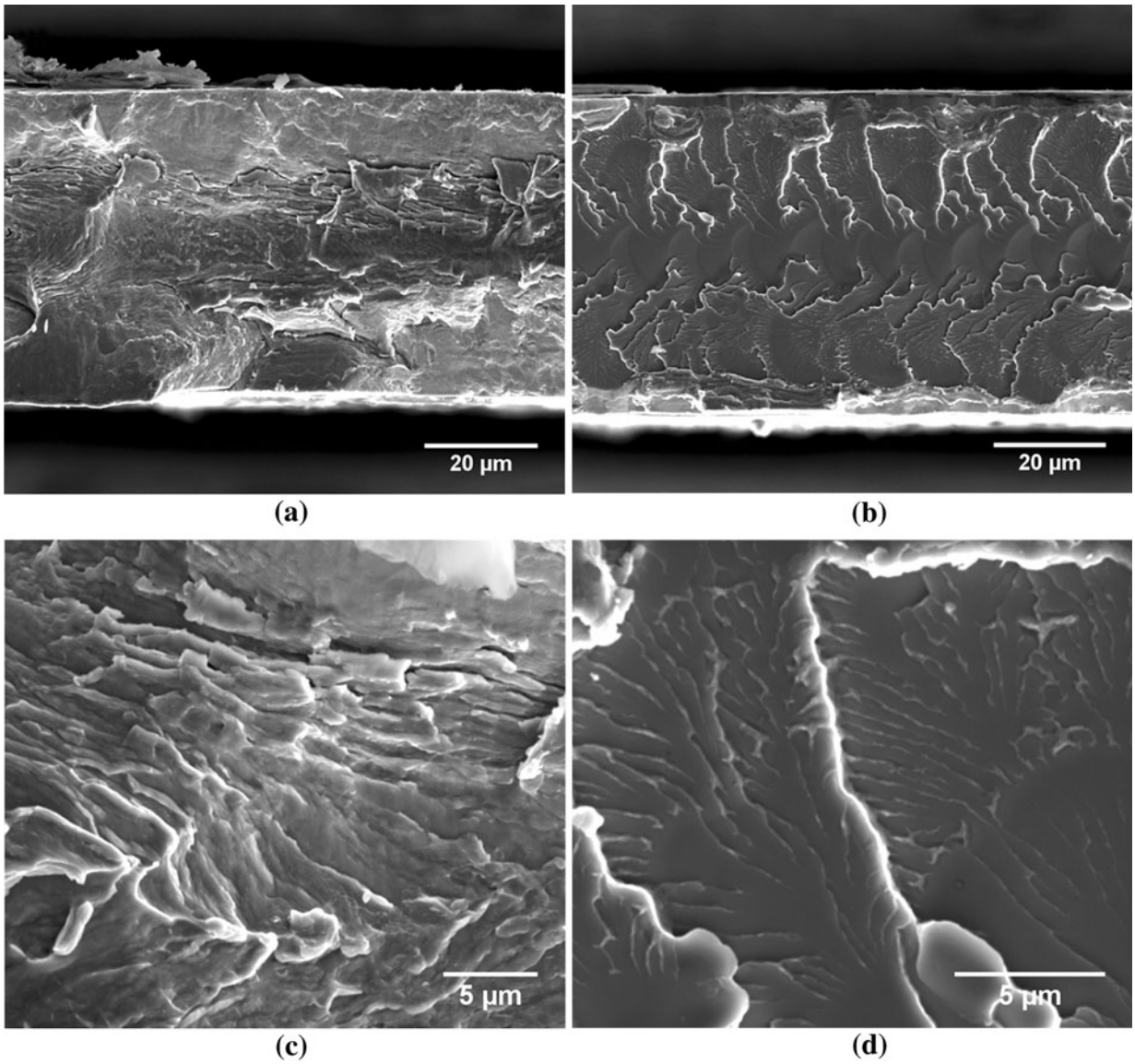

Fig. 2—SEM fatigue fracture surface images of $Al_{86}Gd_6Ni_7Co_1$ ribbon failed after 25,530 cycles. (*a*) Fatigue region, (*b*) overload region, (*c*) higher magnification view of fatigue region, and (*d*) higher magnification view of overload region.

mandrel conditions. In this case, the applied strain range ($\Delta\varepsilon$) can be calculated as $\frac{2t}{D}$ where t is the thickness of the ribbon and D is the mandrel diameter. The derivation is described in detail in other papers.[20] The effects of changes in the applied strain range of on the number of cycles to failure for the Al-Gd-Ni-X (X = Fe or Co) amorphous alloy ribbons is provided in Figure 3 and Table II. As expected, flex bending over a larger diameter mandrel produces a smaller strain range, thereby producing more cycles to failure.

Changes to the alloy ribbon chemistry seem to exhibit a significant effect on the flex bending fatigue life as shown in Figure 3. Multiple experiments were conducted and each datum represents one test to failure, with runouts denoted by arrows for samples that withstood 1,000,000 cycles without failure. An examination of the data reveals that the lowest strength (*i.e.,* from tension, hardness conversion, *etc.*) ribbon

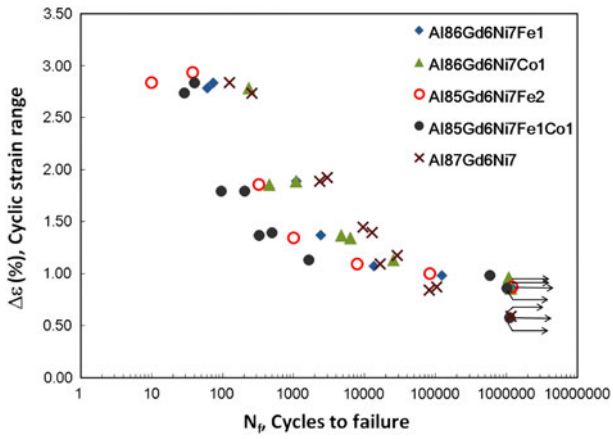

Fig. 3—Flex bending fatigue data in terms of the applied strain range for Al-Gd-Ni-X (X = Fe or Co) amorphous alloy ribbons. The arrows indicate the sample did not fail.

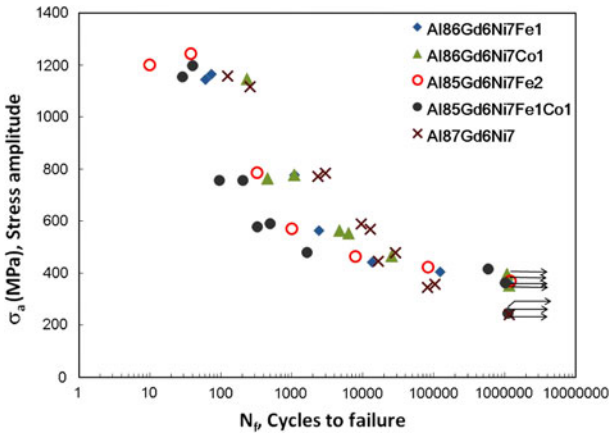

Fig. 4—Flex bending fatigue data in terms of the applied stress amplitude for Al-Gd-Ni-X (X = Fe or Co) amorphous alloy ribbons. The arrows indicate the sample did not fail.

(*i.e.,* $Al_{87}Gd_6Ni_7$) seems to exhibit the best properties under low cycle fatigue conditions but the poorest properties under high cycle fatigue conditions. In contrast, the highest strength (*i.e.,* from hardness conversion) ribbons (*e.g.,* $Al_{85}Gd_6Ni_7Fe_2$ and $Al_{85}Gd_6Ni_7Fe_1Co_1$) exhibited better HCF behavior but failed at a lower number of cycles in the low-cycle fatigue (LCF) regime. Finally, the intermediate strength ribbons (*e.g.,* $Al_{86}Gd_6Ni_7Fe_1$ and $Al_{86}Gd_6Ni_7Co_1$) exhibited the best balance of HCF and LCF behavior, falling somewhere between the extremes exhibited by the lowest strength and highest strength ribbons.

The flex bending over mandrel method used in this study is a strain-based method. Because the addition of Fe/Co increases the elastic moduli of the ribbons as shown in Table I, the results shown in Figure 3 should be converted to cyclic stress amplitude to enable further discussion. Under the current conditions, ribbons with higher elastic modulus subjected to the same applied strain range would experience a higher applied stress amplitude, thereby likely promoting a shorter life. By applying Hooke's law, the applied cyclic strain can be converted into applied stress amplitude (*i.e.,* $\frac{\sigma_{max}-\sigma_{min}}{2}$), enabling the strain-based S-N curve shown in Figure 3 to be converted into the stress-based S-N curve shown in Figure 4. When analyzed in this manner, the modified results show that the absolute magnitude of the stress amplitude at the fatigue limit at 1,000,000 cycles ranged from 240 MPa for the $Al_{86}Gd_6Ni_7Co_1$ material to a maximum of 397 MPa for the $Al_{87}Gd_6Ni_7$ material. Although the HCF behavior of crystalline aluminum alloys is limited typically by the presence of defects (*e.g.,* inclusions, surface defects, *etc.*), the amorphous ribbons tested currently did not typically exhibit a single site of fatigue initiation from a defect. In cases where defect-initiated fatigue was observed (*e.g.,* $Al_{87}Gd_6Ni_7$ ribbons in the HCF regime), this typically occurred at the edge of the ribbon that was slightly thicker in cross-section than the center of the ribbon, as shown in Figure 5(a). To determine the importance of edge-nucleated failure in such samples, a selected group of $Al_{87}Gd_6Ni_7$, $Al_{86}Gd_6Ni_7Fe_1$, and $Al_{86}Gd_6Ni_7Co_2$ ribbons were

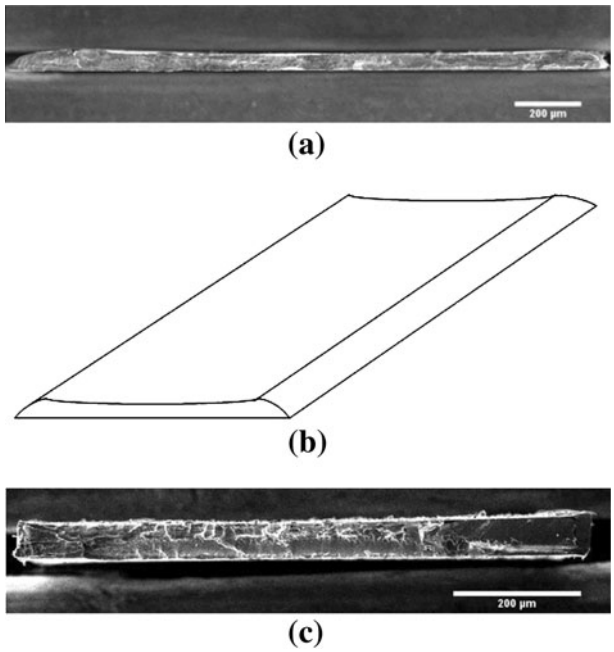

Fig. 5—SEM fatigue fracture surface of cross-sectional area of (*a*) as-received ribbon, (*b*) a schematic of the cross section of a melt-spun ribbon, and (*c*) edge-polished ribbon.

Table IV. Comparison of Fatigue Test Results of As-Received Ribbons *vs.* Edge-Polished Ribbons

Alloy (at. pct)		Mandrel Diameter (mm)	Cycles to Failure (N_f)	Δε (pct)
$Al_{87}Gd_6Ni_7$	As received	12.8	81,089	0.88
	As received	12.8	104,935	0.88
	Edge polished	12.8	66,557	0.88
	Edge polished	12.8	49,250	0.88
$Al_{86}Gd_6Ni_7Co_1$	As received	9.9	25,503	1.13
	Edge polished	9.9	27,819	1.13

polished carefully to remove the raised edges produced by the melt-spinning process. Figure 5(b) shows a schematic of the cross-section of a melt-spun ribbon that exhibits a flat surface on the wheel side (*i.e.,* with surface roughness of 150 nm) in contrast to the concave surface on the air side (*i.e.,* with surface roughness of 40 nm). Figure 5(c) shows the cross-section of the same sample polished to remove the outer edges to produce a ribbon with constant cross-sectional area. These polished samples were then tested in the manner identical to that presented previously for the flex bending fatigue tests, and the results are summarized in Table IV.

The results show that the edge of the ribbon does not have significant influence on the fatigue property.

The samples that received the polishing step to remove the outside edges typically failed at a similar number of cycles to tests conducted on the as melt-spun samples, as summarized in Table IV. Thus, the thicker edges do not seem to influence the fatigue life of the current materials significantly at the strain range used in the current tests.

The quasi-static bend over mandrel tests revealed shear band initiation clearly at strain levels (ε_{max}) of 1.39 pct to 1.40 pct for $Al_{85}Gd_6Ni_7Fe_2$ and $Al_{85}Gd_6Ni_7Fe_1Co_1$ ribbons, Table II. At these levels of applied strain range ($\Delta\varepsilon = 2\varepsilon_{max} = 2.8$ pct) in the flex bending fatigue tests, the fatigue life was only 10 to 76 cycles as shown in Figures 1 and 3 and Table III. Although strain levels significantly smaller than these levels should not produce significant shear banding, the samples failed in flex bending fatigue at cycles that ranged from 1653 to 7828 even when the applied strain range levels was only 1.1 pct ($\Delta\varepsilon = 2\varepsilon_{max} = 1.1$pct). A subsequent reduction in cyclic strain produced larger number of cycles to failure as shown in Figure 1 and Table III. This observation indicates that some nanoscopic and/or microscopic features (*e.g.,* shear-transformation-zone (STZ) and other heterogeneities) must be active to start the process of fatigue in the current materials. Although quantifying the detailed mechanism(s) of microscopic flow in amorphous metals remains elusive and is the subject of continuing research, recent work[27] on cyclical loading of a bulk metallic glass (BMG) via cyclic nanoindentation suggests cyclic hardening in local regions stressed in compression. This phenomenon has been proposed as one of the reasons possibly responsible for the coaxing effect on fatigue that has been reported recently for a BMG.[28] Although the detailed mechanism(s) of such nanohardening are still under discussion, other equation of state (EOS) work[29–31] showed clear differences in the P-V relationship at low pressures *vs* high pressures. This suggests that any transformation of locally "soft" regions triggered prior to macroscopic evidence of shear banding could contribute to the early initiation of fatigue cracks in such amorphous systems. Observations of improved fatigue limits that occur after structural relaxation[28] without devitrification would be consistent with removal of the locally "soft" regions in the metallic glass.

Once the fatigue crack(s) are initiated, crack growth produces features similar to "striations" observed in crystalline metals. In fatigue crack growth, the spacing of such "striations" is dependent on the cyclic stress intensity as it controls the fatigue crack growth rate. Although it is difficult to determine the cyclic stress intensity for the current crack growth conditions, the spacing of "striation-like" features was measured for separate samples of $Al_{85}Gd_6Ni_7Fe_1Co_1$ material tested under low cycle fatigue (*i.e.,* $\Delta\varepsilon = 2.78$pct, $N_f = 234$ cycles) and high cycle fatigue (*i.e.,* $\Delta\varepsilon = 1.13$pct, $N_f = 25{,}530$ cycles) conditions and are summarized in Figure 6. The spacing of the "striation-like" features was measured from the surface of the ribbon in both cases and reveals an increase in spacing with increasing depth toward the midsection of the ribbon in both cases, although the spacings are greater in the sample tested under low cycle fatigue comparison with that exhibited by the sample failing under high cycle fatigue conditions. Although stress intensity solutions are not available for this geometry of sample tested in the current manner, testing under high cycle fatigue conditions at low cyclic stresses will produce relatively low cyclic stress intensities and initially low fatigue crack growth rates that will increase as the crack extends. In contrast, testing under low cycle fatigue conditions at high cyclic stresses will produce greater cyclic stress intensities and higher fatigue crack growth rates that will continue to increase as the crack extends. The results shown in Figure 6 for the increase in spacing with increasing distance from the ribbon surface is consistent with this scenario.

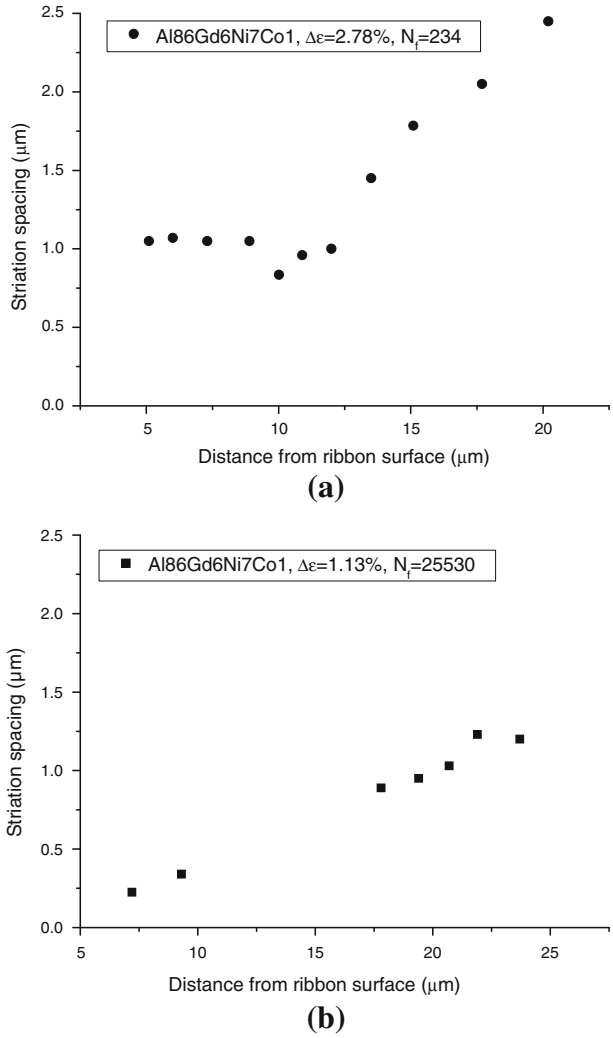

Fig. 6—Measurement of striation spacing from surface of ribbons failed in $R = -1$ flex bending fatigue for (*a*) LCF and (*b*) HCF conditions.

The stress amplitude at the fatigue limits for these Al-Gd-Ni based amorphous alloy ribbons ranged from 240 MPa ($Al_{87}Gd_6Ni_7$) to 397 MPa ($Al_{86}Gd_6Ni_7Co_1$). These values are significantly higher than those of the conventional aluminum alloys. For example, the stress amplitude at the fatigue limit has been reported to be 178 MPa for Al 7075-T6 alloy[32] and 162 MPa for Al 2024-351 alloy[33] for sample tested at uniaxial loading at $R = -1$. In contrast, the fatigue limits for these Al-Gd-Ni based amorphous alloy ribbons are somewhat higher than that reported in bending fatigue at $R = 0.1$ of nanocrystalline aluminum alloys produced from extrusion of amorphous aluminum alloy powders.[6] Other similar work where similar fatigue tests were conducted on $Fe_{78}Si_9B_{13}$ amorphous ribbons produced fatigue limits of 348 MPa, although those ribbons were significantly

stronger and had larger surface roughness in comparison to the present ribbons.[34]

Another approach is to compare the stress amplitude at the fatigue limit to the UTS of the ribbons. This produces the range 0.25 ($Al_{87}Gd_6Ni_7$) to 0.37 ($Al_{86}Gd_6Ni_7Co_1$) for the present materials, in the range of values typically exhibited by conventional aluminum alloys (*i.e.,* 0.31 for Al 7075-T6 and 0.35 for Al 2024-T351).[32,33] These values show that the relative fatigue lifetime and fatigue endurance of Al-Gd-Ni-*X*–based amorphous alloy ribbons are comparable with conventional aluminum alloys, but the absolute magnitude of the stress amplitude is much higher because of their high strength. The amorphous ribbons also exhibit a somewhat higher (stress amplitude/UTS) ratio at the fatigue limit compared with nanocrystalline aluminum alloys produced from extrusion of amorphous aluminum alloy powders (*i.e.,* 0.24 to 0.29).[6] A recent review of the HCF behavior of Zr-based bulk metallic glasses with UTS approaching 2 GPa reveals the stress amplitude at the fatigue limit to range from 70 to 475 MPa depending on *R* ratio, producing a ratio of 0.04 to 0.28 for the Zr-based bulk metallic glass systems.[7,15]

The strain-based fatigue-life behavior showed in Figure 3 has been analyzed according to the Coffin–Manson–Basquin relationship.[35–37] In such a manner, the total applied strain is described by the combination of plastic strain amplitude and elastic strain amplitude and is given by:

$$\frac{\Delta\varepsilon}{2} = \left(\frac{\sigma_f'}{E}\right)(2N_f)^b + \varepsilon_f'(2N_f)^c$$

where $\Delta\varepsilon/2$ is the applied strain amplitude, σ_f' is the fatigue strength coefficient, E is the elastic modulus of the material, N_f is the number of cycles to failure, b is the fatigue strength exponent, ε_f' the fatigue ductility coefficient and c is the fatigue ductility exponent. Figures 7(a) though (e) show the fitted Coffin–Manson–Basquin curves for Al-Gd-Ni–based amorphous alloy ribbons. In order to fit the present data using the Coffin-Manson-Basquin approach, the elastic modulus obtained from instrumented indentations was used. The fitted range for fitting parameters were set to be 0 to –0.3 for b and –0.5 to –1 for c, based on the database generated on conventional structural materials.[35–37] The values for σ_f' were estimated by converting the microhardness to fracture strength via the relation $\sigma_c = \frac{Hv}{3}$. These values were slightly higher than those obtained in tension shown in Table I because of the inherent difficulties of testing low-ductility materials in tension. The fitted results are summarized in Table V.

The fatigue strength exponents, b = –0.07 to –0.10, and fatigue ductility exponents, c = –0.50 to –0.58, fitted from the current data are consistent with those exhibited by most engineering metals. In contrast, the fatigue ductility coefficient ε_f' shows some differences, which range from 0.013 to 0.216. These values are generally higher than the tensile fracture strain listed in Table I and likely result from the high bend ductility of these materials.

Although the current results show clearly that alloying increases the strength and stress amplitude at the fatigue limit of the Al-Gd-Ni ribbons, separate studies have shown that these alloying additions also increase the T_g of the amorphous alloy.[5] Thus, each fatigue test conducted at room temperature was conducted at a different fraction of T_g for each alloy. As shown in other work, the flow stress and deformation behavior is affected sensitively by T/T_g.[38–40] Using room temperature as the test temperature produces the following T/T_g for each alloy tested currently: $Al_{87}Gd_6Ni_7$: 0.676, $Al_{86}Gd_6Ni_7Fe_1$: 0.633, $Al_{86}Gd_6Ni_7Co_1$: 0.625, $Al_{85}Gd_6Ni_7Fe_2$: 0.570, and $Al_{85}Gd_6Ni_7Fe_1Co_1$: 0.571. To compare the fatigue test results at an equivalent T/T_g to eliminate this factor, flex fatigue tests were conducted on the $Al_{87}Gd_6Ni_7$ ribbons at 277 K (4 °C) to produce a T/T_g = 0.628, enabling a direct comparison with the $Al_{86}Gd_6Ni_7Fe_1$ and $Al_{86}Gd_6Ni_7Co_1$ ribbons tested at room temperature with T/T_g = 0.633 and 0.625, respectively.

Prior to flex fatigue testing of the $Al_{87}Gd_6Ni_7$ ribbons at 277 K (4 °C), uniaxial tension tests were conducted at this same temperature to determine whether any test temperature effects were observed on the strength, ductility, *etc.* Multiple samples tested at 277 K (4 °C) in tension revealed that the strength increased approximately 1 pct without changing the ductility, which is consistent with previous work. Tests at much lower temperature might produce more significant strength differences as recent work by Liu *et al.* at 77 K (–196 °C) on a Zr-based glass showed a 16 pct increase in compressive strength compared with 298 K (25 °C).[41] This was rationalized as to the result of decreased thermal vibrations in the glass. Hardness tests at 77 K (–196 °C) for the current material revealed an 8 pct increase in hardness. The flex fatigue behavior of the low-temperature tests compared with room temperature for same alloy are shown in Figure 8. Included on this plot are data from alloys $Al_{86}Gd_6Ni_7Fe_1$ and $Al_{86}Gd_6Ni_7Co_1$, which were tested at room temperature but at similar values of T/T_g (*i.e.,* 0.633 and 0.625) because of their higher T_g. The flex fatigue test result shows that the stress amplitude at the fatigue limit for the $Al_{87}Gd_6Ni_7$ ribbons increases from 240 MPa at room temperature to 372 MPa at 277 K (4 °C) and is close to the HCF behavior of the higher T_g $Al_{86}Gd_6Ni_7Fe_1$ and $Al_{86}Gd_6Ni_7Co_1$ alloys. Fracture surface appearances for the RT and 277 K (4 °C) tests were similar. Thus, contributing reasons for the alloying-induced improvement of the fatigue limit include the alloying-induced increased strength as well as the lower T/T_g ratio for the test at 277 K (4 °C). It is interesting to note the improvement in HCF behavior provided by the 277 K (4 °C) tests occurs without compromising the LCF behavior. More work at different T/T_g will be needed to determine the generality of these observations and the detailed mechanisms responsible for this behavior.

V. CONCLUSIONS

The fatigue behavior of Al-Gd-Ni-*X* (*X* = Fe or Co) amorphous alloy ribbons was evaluated by fully reversed cyclic strain-controlled bending fatigue with

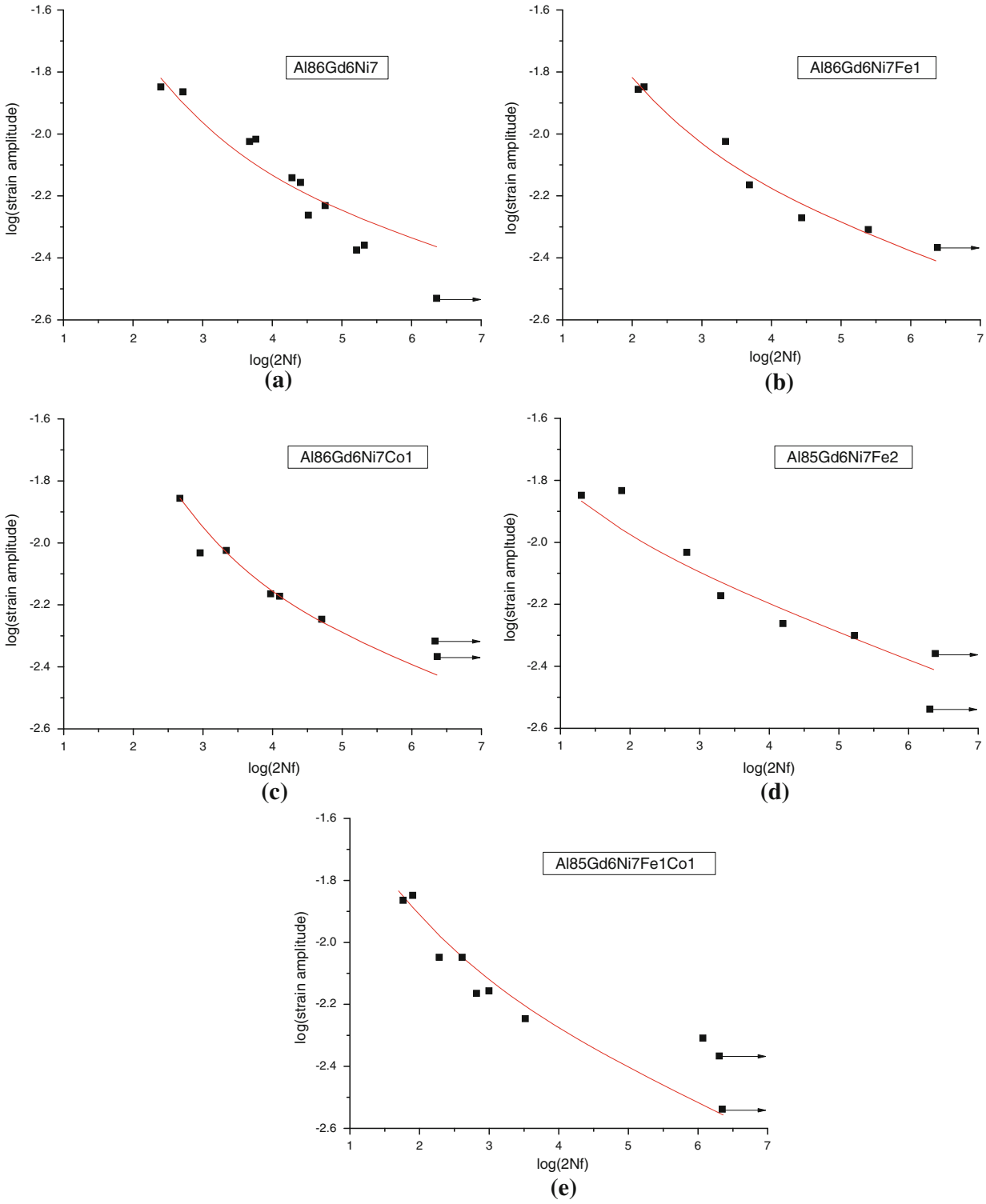

Fig. 7—Best fit of the flex bending fatigue data to the Coffin–Manson–Basquin equation for (*a*) $Al_{87}Gd_6Ni_7$, (*b*) $Al_{86}Gd_6Ni_7Fe_1$,(*c*) $Al_{86}Gd_6Ni_7Co_1$, (*d*) $Al_{85}Gd_6Ni_7Fe_2$, and (e) $Al_{85}Gd_6Ni_7Fe_1Co_1$. The arrows indicate the sample did not fail after 1,000,000 cycles.

the use of a flex bending tester. The applied cyclic strains were controlled by the use of different diameter mandrels. The results obtained are summarized as follows:

1. The flex bending fatigue life of Al-Gd-Ni-*X* (*X* = Fe or Co) amorphous alloy ribbons increased with an increase in mandrel diameter (*i.e.*, decreasing cyclic strain). The SEM fracture surfaces indicated that the fatigue failure started at the both air and wheel surfaces of the ribbon and propagated toward the center. The overload region revealed vein-like features that propagated from the fatigue regions.

Table V. Summary of Fitted Results of Current Fatigue Data via Coffin–Manson–Basquin Relationship

Alloy (at pct)	σ_f'(MPa)	E (GPa)	ε_f'	b	c
$Al_{86}Gd_6Ni_7Fe_1$	1063	82.2	0.064	–0.08	–0.50
$Al_{86}Gd_6Ni_7Co_1$	1079	82.4	0.216	–0.09	–0.58
$Al_{85}Gd_6Ni_7Fe_2$	1076	84.7	0.013	–0.09	–0.50
$Al_{85}Gd_6Ni_7Fe_1Co_1$	1089	84.5	0.043	–0.11	–0.50
$Al_{87}Gd_6Ni_7$	982	81.6	0.110	–0.07	–0.50

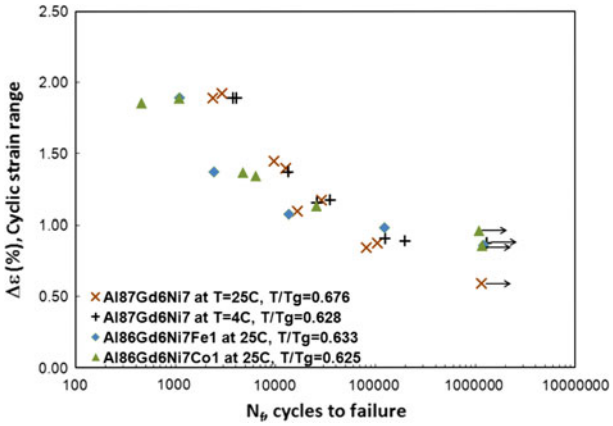

Fig. 8—The comparison of flex bending fatigue data in terms of applied strain range for $Al_{86}Gd_6Ni_7$ ribbon tested at room temperature and 277 K (4 °C) and $Al_{86}Gd_6Ni_7Fe_1$, and $Al_{86}Gd_6Ni_7Co_1$ tested at room temperature. The arrows indicate the sample did not fail after 1,000,000 cycles.

2. The substitution for Al by Fe and Co additions increased the stress amplitude significantly at the fatigue limit. The stress amplitude at the fatigue limit of the ribbons used in the current study ranges from 240 to 397 MPa. These values are higher than most conventional aluminum alloys and are comparable with nanocrystalline aluminum alloys produced from extrusion of amorphous aluminum alloy powders.[6,27,28]
3. The current fatigue results were analyzed by the Coffin–Manson–Basquin relationship. The fatigue strength coefficient *b* and fatigue ductility coefficient *c* were determined, and the fitted values are in the range of those exhibited by most structural metals.
4. Preliminary fatigue tests showed that the stress amplitude at the fatigue limit and HCF behavior of $Al_{87}Gd_6Ni_7$ ribbons improved when tested at low temperature (*i.e.,* low T/T_g ratio), without significantly affecting the LCF regime.

ACKNOWLEDGMENTS

The authors thank the DARPA-SAM 2 program for support through Pratt & Whitney Corporation. The supply of materials from Pratt & Whitney and Ames laboratory is gratefully acknowledged. Useful discussions with A. L. Greer and G. J. Shiflet are also appreciated. Technical support was provided by the MMC group of Case Western Reserve University.

REFERENCES

1. A.L. Greer: *Science*, 1995, vol. 267, p. 1947.
2. A. Inoue, K. Ohtera, A.P. Tsai, and T. Masumoto: *Jpn. J. Appl. Phys.*, 1988, vol. 27, p. 280.
3. Y. He, S.J. Poon, and G.J. Shiflet: *Science*, 1988, vol. 241, p. 1640.
4. A. Inoue, S. Sobu, D.V. Louzguine, H. Kimura, and K. Sasamori: *J. Mater. Res.*, 2004, vol. 19, p. 1539.
5. C.K. Huang and J.J. Lewandowski: *Metall. Mater. Trans. A*, 2010, vol. 41A, p. 2269.
6. A.B. El-Shabasy, H.A. Hassan, Y. Liu, D. Li, and J.J. Lewandowski: *Mater. Sci. Eng. A*, 2009, vols. 513–514, p. 202.
7. C.J. Gilbert, J.M. Lippmann, and R.O. Ritchie: *Scripta Mater.*, 1998, vol. 38, p. 537.
8. C.J. Gilbert, V. Schroeder, and R.O. Ritchie: *Metall. Mater. Trans. A*, 1999, vol. 39A, p. 1739.
9. W.H. Peter, P.K. Liaw, R.A. Buchanan, C.T. Liu, C.R. Brooks, J.A. Horton, C.A. Carmichael, and J.L. Wright: *Intermetallics*, 2002, vol. 10, p. 1125.
10. W.H. Peter, R.A. Buchanan, C.T. Liu, and P.K. Liaw: *J. Non-Cryst. Solid*, 2003, vol. 317, p. 187.
11. R. Yavari, J.J. Lewandowski, and J. Eckert: *J. Mater. Res.*, 2007, vol. 22, p. 255.
12. G.Y. Wang, P.K. Liaw, A. Peter, M. Freels, W.H. Peter, R.A. Buchanan, and C.R. Brooks: *Intermetallics*, 2006, vol. 14, p. 1091.
13. Y. Yokoyama, P.K. Liaw, M. Nishijima, K. Hiraga, R.A. Buchanan, and A. Inoue: *Mater. Trans.*, 2006, vol. 47, p. 1286.
14. G.Y. Wang, D.C. Qiao, Y. Yokoyama, M. Freels, A. Inoue, and P.K. Liaw: *J. Alloys Compd.*, 2009, vol. 483, p. 143.
15. G.Y. Wang, P.K. Liaw, and M.L. Morrison: *Intermetallics*, 2009, vol. 17, p. 579.
16. J.A. Verduzco, R.J. Hand, and H.A. Davies: *Int. J. Fatigue*, 2004, vol. 24, p. 1089.
17. ASTM E 796-94, Standard Test Method for Ductility Testing of Metallic Foil, in *1999 Annual Book of ASTM Standards*, vol. 03.01, ASTM, Philadelphia, PA.
18. H.D. Merchant, M.G. Minor, and Y.L. Liu: *J. Electron. Mater.*, 1999, vol. 28, p. 998.
19. H.D. Merchant, J.T. Wang, L.A. Glannuzzi, and Y.L. Liu: *Circ. World*, 2000, vol. 26, p. 7.
20. J.J. Lewandowski, R. Varadarajan, B. Smith, C. Tuma, M. Shazly, and L.O. Vatamanu: *Mater. Sci. Eng. A*, 2008, vol. 486, p. 447.
21. J. Caris, R. Varadarajan, J.J. Stephens Jr., and J.J. Lewandowski: *Mater. Sci. Eng. A*, 2008, vol. 491, p. 137.
22. J.J. Lewandowski, R. Varadarajan, and B. Smith: *Mater. Sci. Eng. A*, 2008, vol. 492, p. 191.
23. Y. Zhang and A.L. Greer: *J. Alloys Compd.*, 2007, vols. 434–438, p. 2.
24. W.H. Wang, P. Wen, Y. Zhang, M.X. Pan, and R. Wang: *Appl. Phys. Lett.*, 2001, vol. 79, p. 3947.
25. R.D. Conner, W.L. Johnson, N.E. Paton, and W.D. Nix: *J. Appl. Phys.*, 2003, vol. 94, p. 904.
26. R.D. Conner, Y. Li, W.D. Nix, and W.L. Johnson: *Acta Mater.*, 2004, vol. 52, p. 2429.
27. C.E. Packard, L.M. Witmer, and C.A. Schuh: *Appl. Phys. Lett.*, 2008, vol. 92, p. 171911.
28. A.B. El-Shabasy and J.J. Lewandowski: *Scripta Mater.*, 2010, vol. 62, p. 1708.
29. W.H. Wang, P. Wen, L.M. Wang, Y. Zhang, M.X. Pan, D.Q. Zhao, and R.J. Wang: *Appl. Phys. Lett.*, 2001, vol. 79, p. 3947.
30. W.H. Wang, R.J. Wang, D.Q. Zhao, M.X. Pan, and Y.S. Yao: *Phys. Rev. B*, 2000, vol. 62, p. 11292.
31. Y. Guo and M. Li: *J. Appl. Phys.*, 2010, vol. 108, p. 113510.
32. A. Carpinteri and R. Brighenti: *J. Mater. Sci.*, 2008, vol. 43, p. 4780.
33. R. Jurcevic, D.L. DuQuesnay, T.H. Topper, and M.A. Pompetzki: *Int. J. Fatigue*, 1990, vol. 12, p. 259.
34. A.B. El-Shabasy and J.J. Lewandowski: *Metall. Mater. Trans. A*, in press.

35. S.S. Manson: National Advisory Commission on Aeronautics: Report 1170, Lewis Flight Propulsion Laboratory, Cleveland, OH, 1954.
36. L.F. Coffin: *Trans. AIME*, 1954, vol. 76, p. 931.
37. S.S. Manson and M.H. Hirschberg: *Fatigue: An Interdisciplinary Approach*, Syracuse University Press, Syracuse, NY, 1964.
38. A.H. Vormelker, O.L. Vatamanu, L. Kecskes, and J.J. Lewandowski: *Metall. Mater. Trans. A*, 2008, vol. 39A, p. 1922.
39. H.A. Hassan, L. Kecskes, and J.J. Lewandowski: *Metall. Mater. Trans. A*, 2008, vol. 39A, p. 2077.
40. F. Spaepen: *Acta Mater.*, 1977, vol. 25, p. 407.
41. C. Fan, P.K. Liaw, V. Hass, J.J. Wall, H. Choo, A. Inoue, and C.T. Liu: *Phys. Rev. B*, 2006, vol. 74, p. 014205.